SUPPORTING INFORMATION FOR

# Asymmetry in the Ligand Coordination Sphere of the [FeFe] Hydrogenase Active Site Is Reflected in the Magnetic Spin Interactions of the Aza-propanedithiolate Ligand

Edward J. Reijerse,[*,†,⊥] Vladimir Pelmenschikov,[*,‡,⊥] James A. Birrell,[†] Casseday P. Richers,[§] Martin Kaupp,[‡] Thomas B. Rauchfuss,[§] Stephen P. Cramer,[‖] and Wolfgang Lubitz[†]

[†]Max-Planck-Institut für Chemische Energiekonversion, Stiftstrasse 34-36, 45470 Mülheim an der Ruhr, Germany

[‡]Institut für Chemie, Technische Universität Berlin, Strasse des 17 Juni 135, 10623 Berlin, Germany

[§]School of Chemical Sciences, University of Illinois, 600 South Mathews Ave, Urbana, Illinois 61801, USA

[‖]SETI Institute, 189 Bernardo Avenue, Mountain View, California 94043, United States

**Table of Contents** **Page**

**A. A new synthetic route for the $^{57}$Fe labeled ADT precursor** **S2**

**B. Experimental and computational procedures** **S3**

**C. Supplementary Figures** **S7**

**D. Supplementary Tables** **S16**

**References** **S18**

## A. A new synthetic route for the $^{57}$Fe labeled ADT precursor

A new simplified synthesis for the triply labeled precursor complex $^{57}Fe_2(CN)_2(CO)_3(^{13}C^2H\text{-}ADT)$ was developed for on-going NRVS experiments. Previously, $^{57}$Fe-labeled complexes were prepared by the conversion of $^{57}FeCl_2$ to $^{57}Fe_2(S_2)(CO)_6$ (Scheme S1). The $^{57}Fe_2(S_2)(CO)_6$ was subsequently converted to $^{57}Fe_2(ADT)(CO)_6$ in 30% yield, followed by installation of the pair of cyanide cofactors. In the new method, $^{57}FeCl_2$ was found to undergo reductive carbonylation in the presence of the protected version of ADT, $CbzN(CH_2SH)_2$. Perhaps because it is relatively rigid, $CbzN(CH_2SH)_2$ is a particularly efficient precursor, giving $^{57}Fe_2((SCH_2)_2NCbz)(CO)_6$ in 40% yield. Amine deprotection was effected with $BF_3$ to give $Fe_2((SCH_2)_2NH)(CO)_6$.[1]

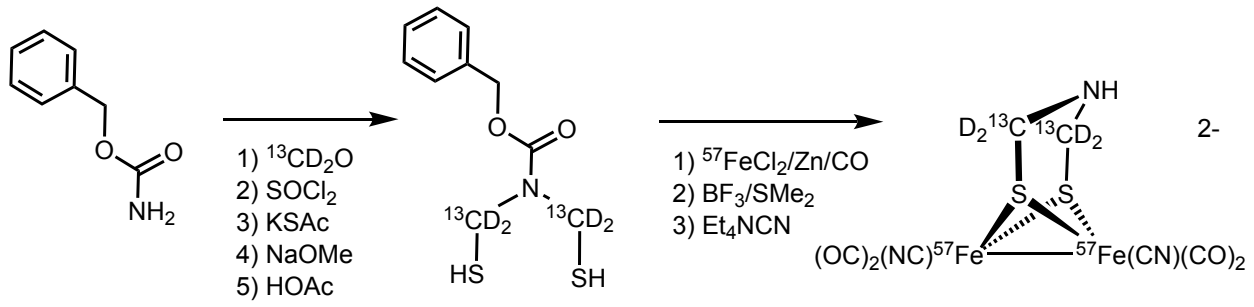


**Scheme S1.** Synthesis of isotope labeled $[2Fe]_H$ precursor.

## B. Experimental and computational procedures

1. Synthesis of $[2Fe]_H$ precursor

**$^{57}Fe_2[(SCH_2)_2NCbz](CO)_6$.** A THF (50 mL) suspension of $^{57}FeCl_2$ (700. mg, 5.47 x $10^{-3}$ mol) was treated with a THF (10 mL) solution of $CbzN(CH_2SH)_2$ (666 mg, 2.74 x $10^{-3}$ mol). The mixture was sparged with CO and $NEt_3$ (759 µL, 554 mg, 5.47 x $10^{-3}$ mol) was added. The mixture became reddish-brown. The septum on the reaction flask was removed, and zinc powder (1.8 g, 2.7 x 10-2 mol) was added as a solid. The septum was replaced, and the reaction was stirred at room temperature under a constant pressure of CO (1 atm). After 48 h, the reaction mixture was opened to the air, filtered through Celite, and evaporated using a rotary evaporator. The residual solid was extracted into a 80:20 mixture of hexanes:EtOAc, and this extract was filtered through a plug of silica gel. A red band was collected and evaporated yielding a red solid. Yield: 580 mg, 1.1 x $10^{-3}$ mol (40%). A completely analogous procedure was used to prepare octa-labeled $^{57}Fe_2[(S^{13}C^2H_2)_2NCbz](CO)_6$.

**Deprotection of $Fe_2[(SCH_2)_2NCbz](CO)_6$ with $BF_3{\cdot}OEt_2$ and $Me_2S$.** A solution of $Fe_2[(SCH_2)_2NCbz](CO)_6$ (47 mg, 9.02 x $10^{-5}$ mol) in $CH_2Cl_2$ (5 mL) was treated with $Me_2S$ (198 µL, 168 mg, 2.71 x $10^{-3}$ mol) and $BF_3{\cdot}OEt_2$ (111 µL, 128 mg, 9.02 x $10^{-4}$ mol) under a nitrogen atmosphere. The mixture was stirred at room temperature for 5 h before quenching with $H_2O$ (5 mL) added under ambient conditions. The organic and aqueous phases were separated, and the aqueous phase was extracted with additional $CH_2Cl_2$ (2 x 5 mL). The organic extracts were combined, dried over $MgSO_4$, and concentrated to red solid. This residue was purified by column chromatography ($CH_2Cl_2$, $R_f$ = 0.50). Yield: 27 mg, 6.98 x $10^{-5}$ mol (77%). Spectroscopic data matched those for $Fe_2(ADT)(CO)_6$. $^{57}Fe_2(ADT)(CO)_6$ and $[^{57}Fe_2[(S^{13}C^2H_2)_2NCbz](CO)_6$ were prepared analogously.

**$(Et_4N)_2[^{57}Fe_2(ADT)(CN)_2(CO)_4]$ and $(Et_4N)_2[^{57}Fe_2[(S^{13}C^2H_2)_2NH](CN)_2(CO)_4]$.** A MeCN (3 mL) solution of $^{57}Fe_2(ADT)(CO)_6$ (304 mg, 7.81 x $10^{-4}$ mol) was treated with a MeCN (1 mL) solution of $(Et_4N)CN$ (244 mg, 1.56 x $10^{-3}$ mol). A gas immediately evolved. The reaction was stirred at room temperature, its progress monitored by IR spectroscopy. After 12 h the reaction was complete and the solvent was removed under vacuum. A red oily solid was obtained. The solid was agitated or extracted with THF until the extracts no longer appeared yellow and the solid no longer appeared oily. The solid was then washed with $Et_2O$ and dried under vacuum. Yield: red solid, 385 mg, 5.96 x $10^{-4}$ mol (76%). The compound was identified by comparison with literature FT-IR and $^{13}C$ NMR spectra. A completely analogous procedure was used to prepare $(Et_4N)_2[^{57}Fe_2[(S^{13}C^2H_2)_2NH](CN)_2(CO)_4]$.

## 2. Enzyme purification and maturation

Heterologous production of HydA1 from *Chlamydomonas reinhardtii* in *E.coli* and artificial maturation of the H-cluster were based on a previously published protocol with minor modifications.[2] The pH was adjusted prior to induction of the protein expression and the purification was performed without any dithionite. 100 mg/mL Ampicillin and 50 mg/L Kanamycin were used as selection antibiotics throughout the expression. For the maturation the apo-protein was diluted to about 350 µM in 0.1 M Tris/HCl, 0.15 M NaCl pH 8.0. The $(Et_4N)_2[^{57}Fe_2[(S^{13}C^2H_2)_2NH]\ (CO)_2(CO)_4]$ precursor was dissolved in DMSO or $H_2O$ and added as a 2-3 times excess for 60 min. Unbound complexes were removed by a desalting column (PD-10, GE Healthcare) and the maturated proteins were concentrated (Merck Millipore, Amicon Ultra-15, 30 kDa).

## 3. FTIR spectroscopy

FTIR spectra were obtained using an IFS 66v FTIR spectrometer from Bruker Optics with a $N_2$ cooled mercury cadmium telluride (MCT) detector. Sample preparations and measurements were carried out under anaerobic conditions. Samples were placed between $CaF_2$ windows and placed in an air-tight sample holder. The sample chamber of the FTIR spectrometers were continuously purged with dry nitrogen. Spectra were recorded at 15 $^oC$ with 20 kHz velocity in double-sided forward backward mode with phase resolution of 16, zero filling factor of 2 and Blackman-Harris-3-term apodization, and are the average of 1000 scans. Data processing was performed using home-written scripts in the Matlab® programming environment.

## 4. EPR & Pulse ENDOR spectroscopy

Field swept Q-band EPR spectra were obtained on a Bruker ELEXYS E-580 X-band spectrometer equipped with a home-built Q-band accessory with 10W available power at 34 GHz using a home built resonator described earlier.[3] The spectra were recorded in pulsed mode using FID detection after a 1µs $\pi/2$ excitation pulse. After a pseudo-modulation transformation, the spectra obtained in this way are comparable to those obtained using CW EPR.[4] Cryogenic temperatures (10-20 K) were obtained using a liquid helium cooled Oxford CF935 flow cryostat. ENDOR experiments were performed with the same setup making use of a water cooled 400W Bonn-Electronic RF amplifier with frequency range 0.1 - 400 MHz (BSA 1025-400). A Trilithic™ H4LE35-3-AA-R high-power low pass filter (cutoff frequency around 35 MHz) was used to suppress the "harmonics" of the $^1H$ ENDOR signals.

Electron nuclear double resonance (ENDOR) was used to study the $^{13}C$ hyperfine interactions. In this investigation the Mims ENDOR sequence was used: [π/2]-τ-[π/2]-$t_d$-(RF)-$t_d$-[π/2]-τ-(ESE).[5] The excitation of nuclear spin transitions is detectable through a decrease in the ESE intensity. The (π/2) pulses were set to 20 ns and the τ delay to 200 ns. The RF pulses had a length of 60 µs. The extra delay time $t_d$ was kept at 5 µs. For the triple ENDOR experiment, the following sequence was used: [π/2]-τ-[π/2]-$t_d$-($RF_2$)-$t_d$-($RF_1$)-$t_d$-[π/2]-τ-(ESE) (see Scheme S2).[6] Here, the frequency of RF1 is fixed at a certain frequency (a specific ENDOR transition) while RF2 is swept in the usual way.

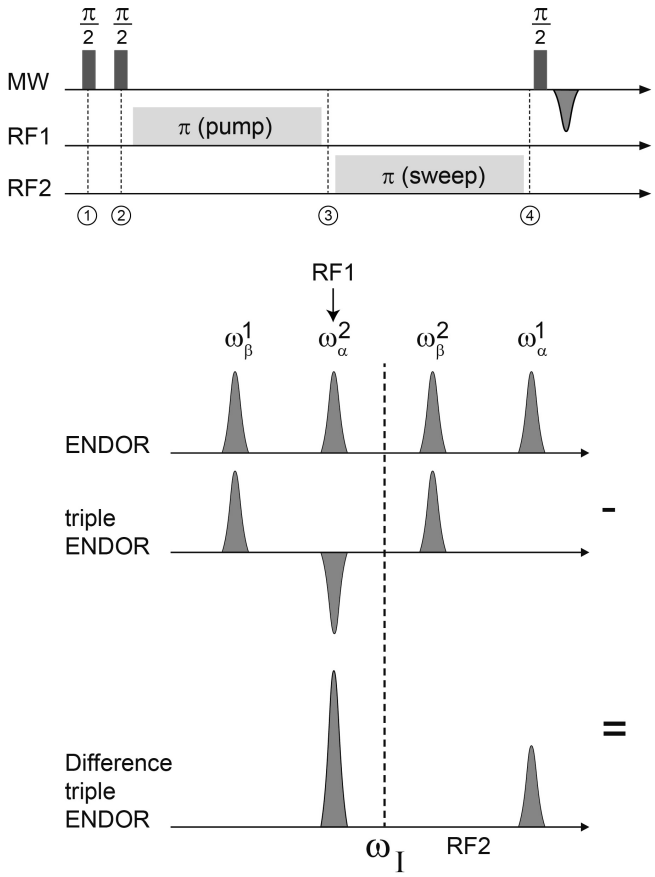


**Scheme S2.** Mims triple resonance experiment. The two HFI couplings (1 and 2) have opposite sign. The RF1 pulse inverts the population of the $\omega^2$ transition in the α-manifold. This reduces the population difference of the $\omega^1$ transition in the same (α) manifold but does not affect the populations in the β-manifold. In the difference triple resonance spectrum, the $\omega^1{}_\alpha$ transition appears as a weak positive contribution and the pumped $\omega^2{}_\alpha$ transition as a strong positive contribution.

## 5. ENDOR simulations and fitting

The orientation selective $^{13}C$ Mims ENDOR spectra were analyzed using first order perturbation theory to calculate the ENDOR profiles. For this, the "sugar" script in Kazan-Viewer (https://sites.google.com/site/silakovalexey/kazan-viewer/) was employed. This script is analogous to the "salt" routine in Easyspin (using the 1st order perturbation option). The ENDOR profiles were scaled by taking the $\tau$-dependence of the ENDOR amplitudes ($1-\cos(2\pi A\tau)$) into account. Automatic fitting was accomplished using a home written script based on the local minimizer "fminsearch" in Matlab. Although the ENDOR amplitudes were corrected for $\tau$-dependence, the resulting fits were non-optimal and individual scaling of the two components was employed to improve the fit. In Figure S4 the decomposed simulations are presented along with the relative scaling factors of the two $^{13}C$ components. At a few field positions where the ENDOR spectrum shows a very broad response (e.g. at 1205.4 mT) the relative scaling of the component strongly deviates from unity suggesting a non-unique fit. We assume, however, that these deviations do not have a large impact on the final fitting parameters.

## 6. DFT calculations

The $[2Fe]_H$ subcluster modeling and the DFT methodology mostly follows our setup denoted earlier as *S* (*S*mall),[7-8] where only the immediate ligands to the two $Fe_{p/d}$ iron sites are included. In the $H_{ox}$ state these are namely 3xCO, 2x$CN^-$, ADT (–NH–), and the cysteine side-chain modeled as $CH_3$-$CH_2$-SH thiol, with the $Fe_p$-bound sulfur protonated mimicking effects from the $[4Fe–4Fe]_H$ subcluster. The structural optimizations and subsequent analyses were done using GAUSSIAN 09[9] employing the B3LYP[10-13] functional, initially based on the densities exported from single point calculations using JAGUAR 9.4,[14] which provided a high-quality initial guess. The LACV3P** basis set as implemented in JAGUAR was employed. For the first- and second-row elements, LACV3P** implies 6-311G** triple-**ζ** basis sets including polarization functions. For the Fe atoms, LACV3P** consists of a triple-**ζ** basis set for the outermost core and valence orbitals, and the quasi-relativistic Los Alamos effective core potential (ECP) for the innermost electrons. The model environment was considered using a self-consistent reaction field (SCRF) polarizable continuum model and integral equation formalism (IEF-PCM)[15] as implemented in GAUSSIAN, with the static dielectric constant set to $\varepsilon = 4.0$ as often used for proteins, and the remaining IEF-PCM parameters at their default values for water. The electronic densities were visualized using GaussView of GAUSSIAN; in this density analysis, *corresponding* singly occupied molecular orbitals (SOMO) were used, based on the in-program biorthogonalization of the occupied canonical α and β MOs to maximally pair electrons of opposite spin. The $^{13}C$ HFI anisotropy vectors in the molecular framework were generated using ChemCraft.[16]

## C. Supplementary Figures

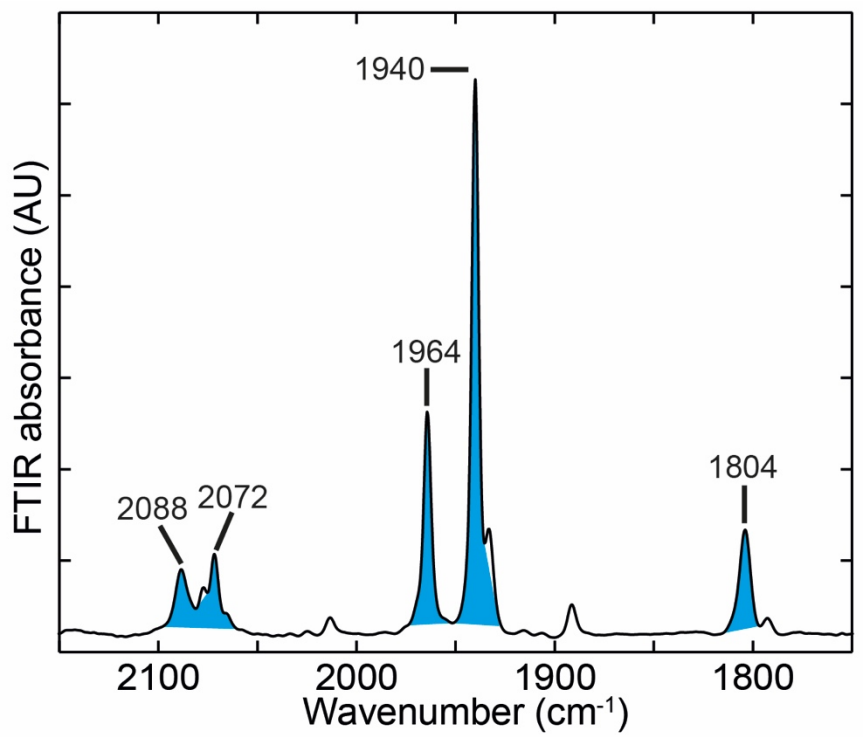


**Figure S1**. FTIR of triply labelled *Cr*HydA1 in the $H_{ox}$ state. A sample (10 µL, 1 mM) of *Cr*HydA1 maturated with $^{13}C^{2}H$-labelled $[2Fe]_H$ precursor was poised in the $H_{ox}$ state under 100 % $N_2$ before transfer between the $CaF_2$ windows of an FTIR cell. The measurement was performed at 15 $^{o}C$ on a Bruker IFS 66v spectrometer, and is the average of 1000 scans. The bands assigned to the $H_{ox}$ state are indicated in blue.

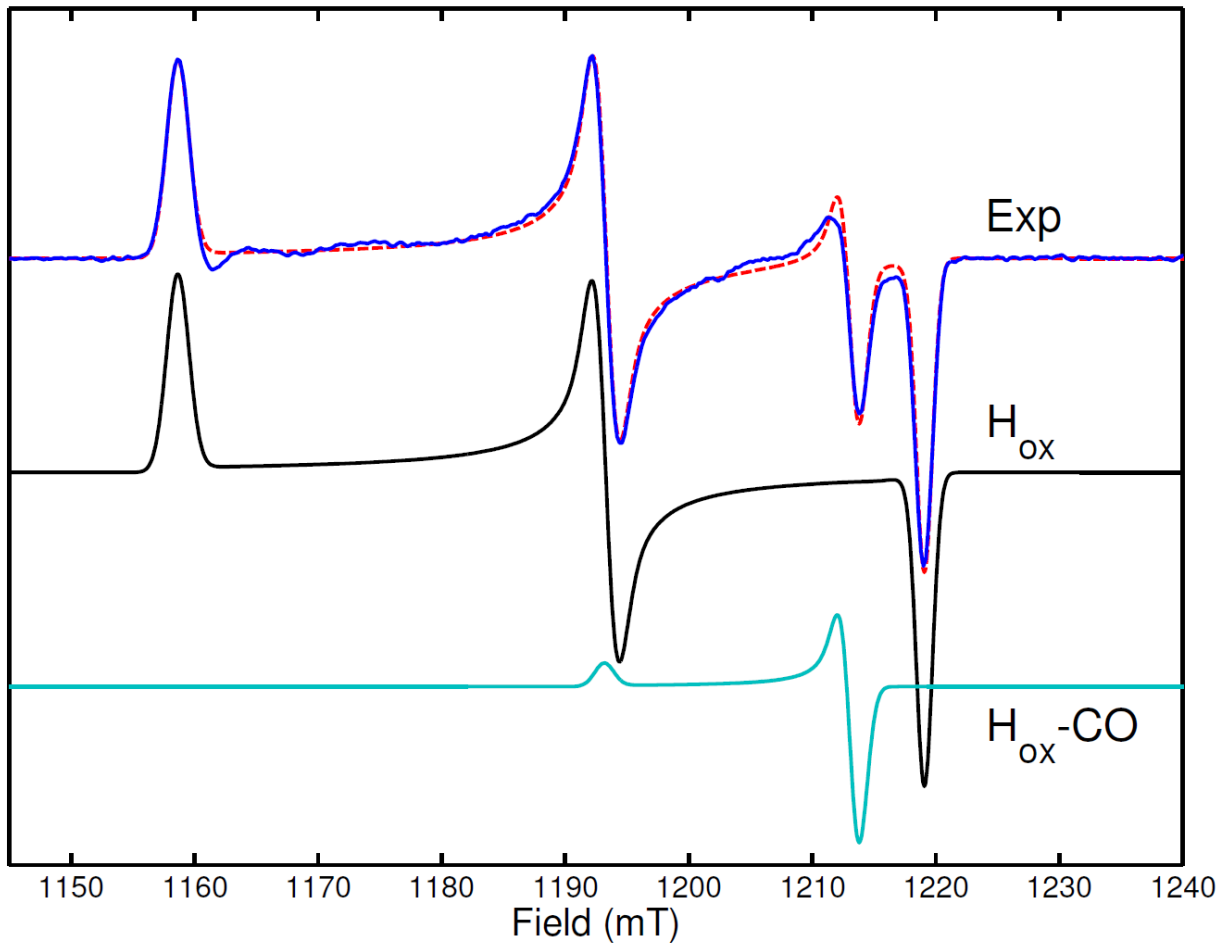


**Figure S2**. Q-band EPR (pseudo-modulated FID detected) of the *Cr*HydA1 $H_{ox}$ state. The field axis was calibrated using a Bruker NMR Gaussmeter. The g-values were obtained through spectral fitting in EasySpin (esfit)[17]: g = (2.1008, 2.0398, 1.9966) for $H_{ox}$ and g = (2.05, 2.006, 2.006) for the contribution from $H_{ox}$-CO (4.4%). MW frequency = 34.0674 GHz.

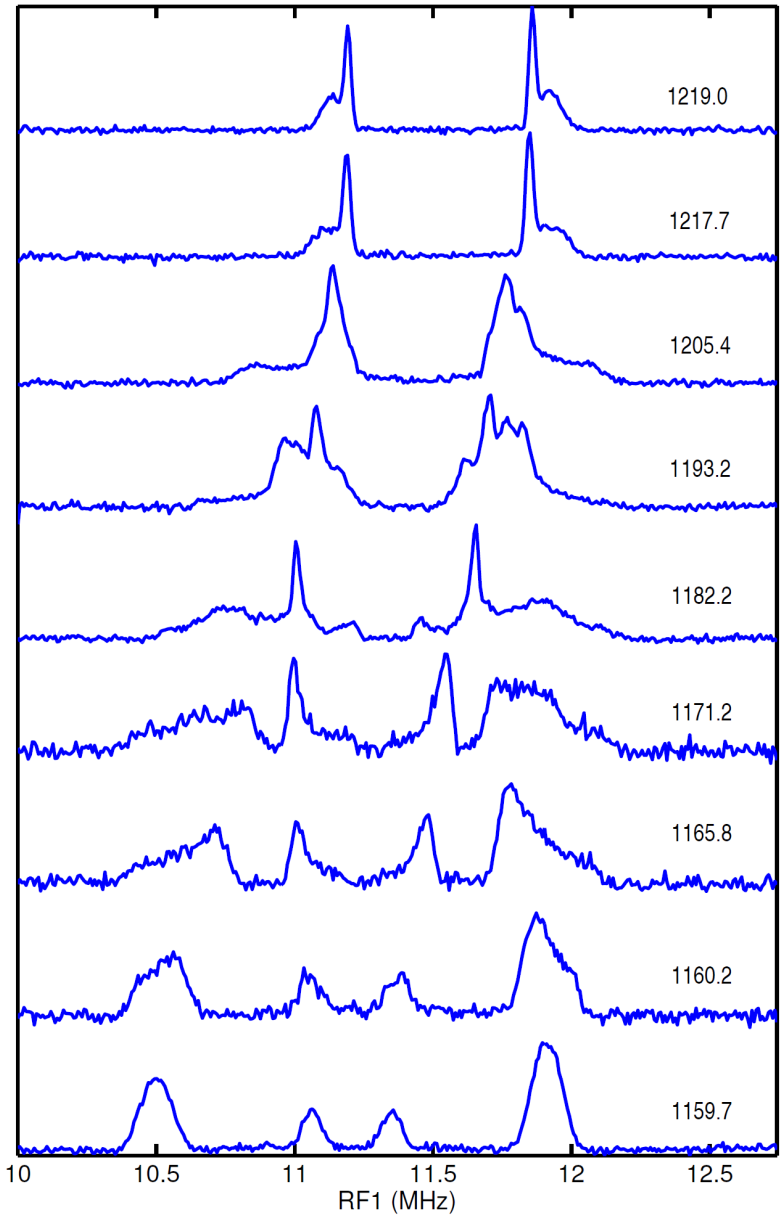


**Figure S3.** Q-band $^{13}$C-Mims-ENDOR data normalized, unsymmetrized. The magnetic field at which each spectrum is recorded is indicated in mT. Temperature 15K, $\tau$ = 200 ns, $\pi/2$ pulse = 20ns, RF pulse = 60 µs. The spectra were recorded with varying number of scans. From low field to high field the scan numbers are: [2000, 200, 200, 100, 300, 100, 180, 50, 200].

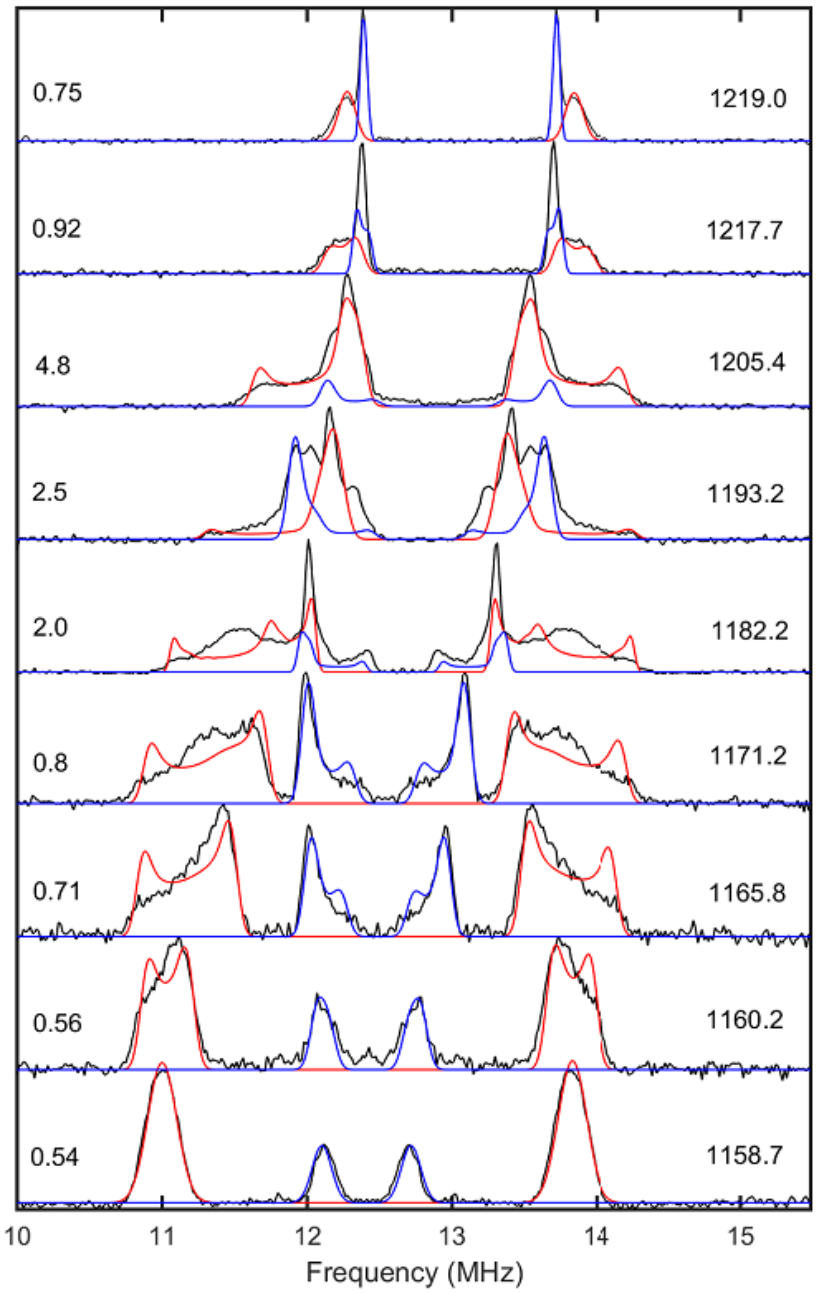


**Figure S4.** $^{13}$C Mims ENDOR Simulations decomposed into the two individual $^{13}$C contributions. The black traces represent the symmetrized experimental spectra. The large positive HFI doublet of the "left" nucleus is displayed in red while the small $^{13}$C HFI component ('right nucleus') is shown in blue. The Mims intensity profile ($1-\cos(2\pi A\tau)$), was taken into account. Here, "A" represents the HFI interaction and $\tau$ was set to 200ns. During the fitting procedure, the two components were individually scaled. The ratios of the scalings of the "red" and "blue" contributions (red/blue) is indicated on the left. Fitting parameters were: HFI(1) = [1.2989 1.0066 3.3008] MHz, EulerAngles(1) = [34.6 28.5 -14.5] degrees. HFI(2) = [-1.4856 -1.7516 -0.44915] MHz, EulerAngles(2) = [0 23 0] degrees.

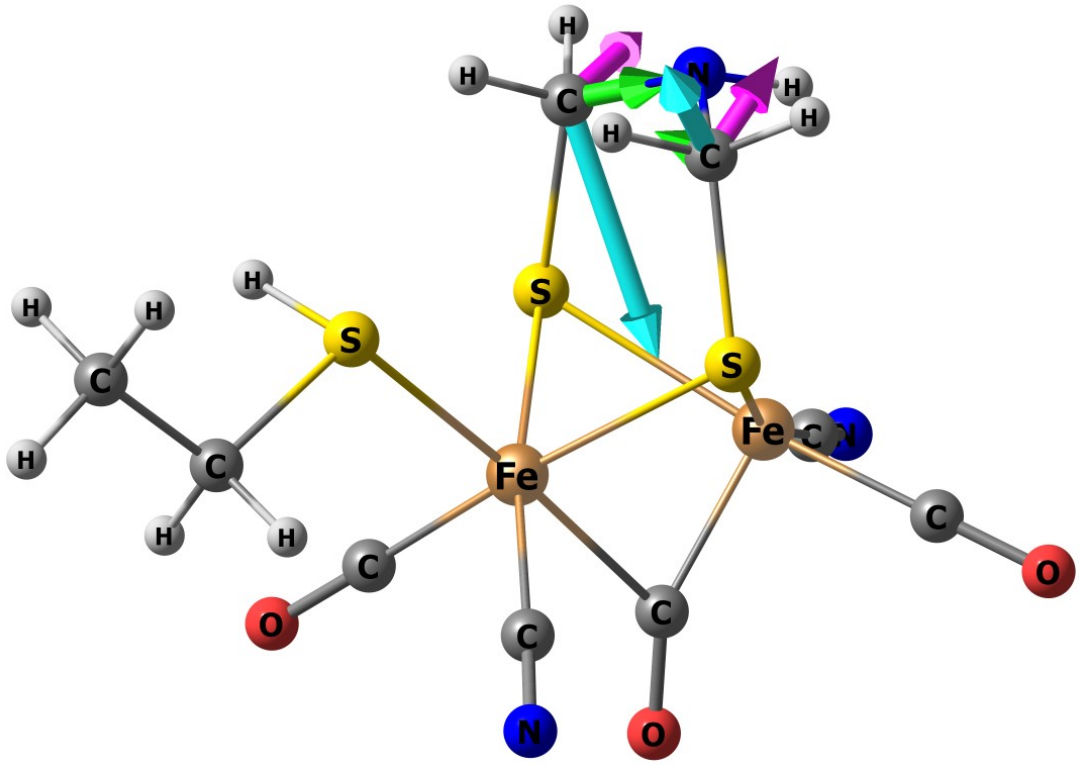


**Figure S5.** Representative DFT model $A_{native}$ of the $H_{ox}$ state with its 'A' = axial orientation of the ADT amine proton. Arrows indicate the two ADT methylene $^{13}C$ anisotropic (excluding the isotropic part) spin dipole HFI tensor orientation as predicted by this model within its molecular framework. The vector lengths correspond to the conversion factor = 2Å/MHz, and the X/Y/Z axis (cf. Table S1) is colored in magenta/green/cyan, correspondingly. In Figure S7, this model $A_{native}$ is shown centrally ≈90° rotated, together with its isomeric alternatives.

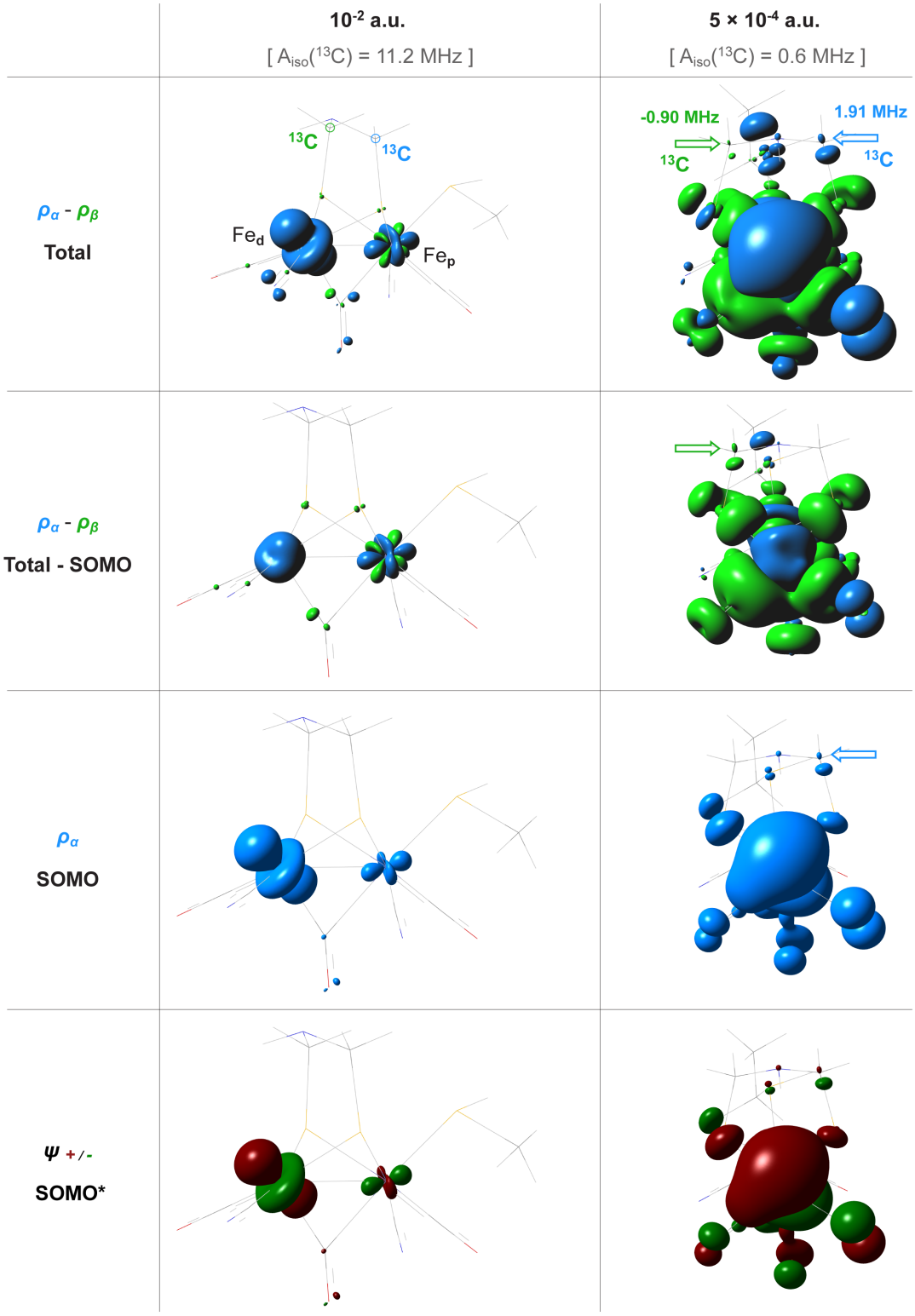


**Figure S6.** Isosurfaces of spin density at $10^{-2}$ and $5\times10^{-4}$ a.u. (corresponding to $A_{iso}(^{13}C)$ = 11.2 and 0.6 MHz) for the representative $H_{ox}$ $S$ = 1/2 DFT model $A_{native}$, with the model itself shown in thin wire. In the $5\times10^{-4}$ vs $10^{-2}$ a.u. images the system is viewed ~90° rotated, from the side of the open coordination site at $Fe_d$ (cf. Figure S7). Shown top to bottom are '*Total*' (integrating to unity, or one unpaired electron), '*Total-SOMO*' (integrating to zero), and *SOMO* (integrating to unity) spin densities; the *SOMO* orbital itself (*) is additionally shown (using unsquared a.u. contour values). Blue/green lobes represent correspondingly positive/negative spin densities. The *SOMO* has its main contribution from the $Fe_d$ $3d_{z^2}$ orbital ($10^{-2}$ a.u.) and shows its delocalization to the right-side ADT $^{13}C$ nucleus ($5\times10^{-4}$ a.u., blue arrow). The *Total-SOMO* density corresponds to the pure spin polarization effects, producing the negative spin density at the left-side ADT $^{13}C$ nucleus ($5\times10^{-4}$ a.u., green arrow).

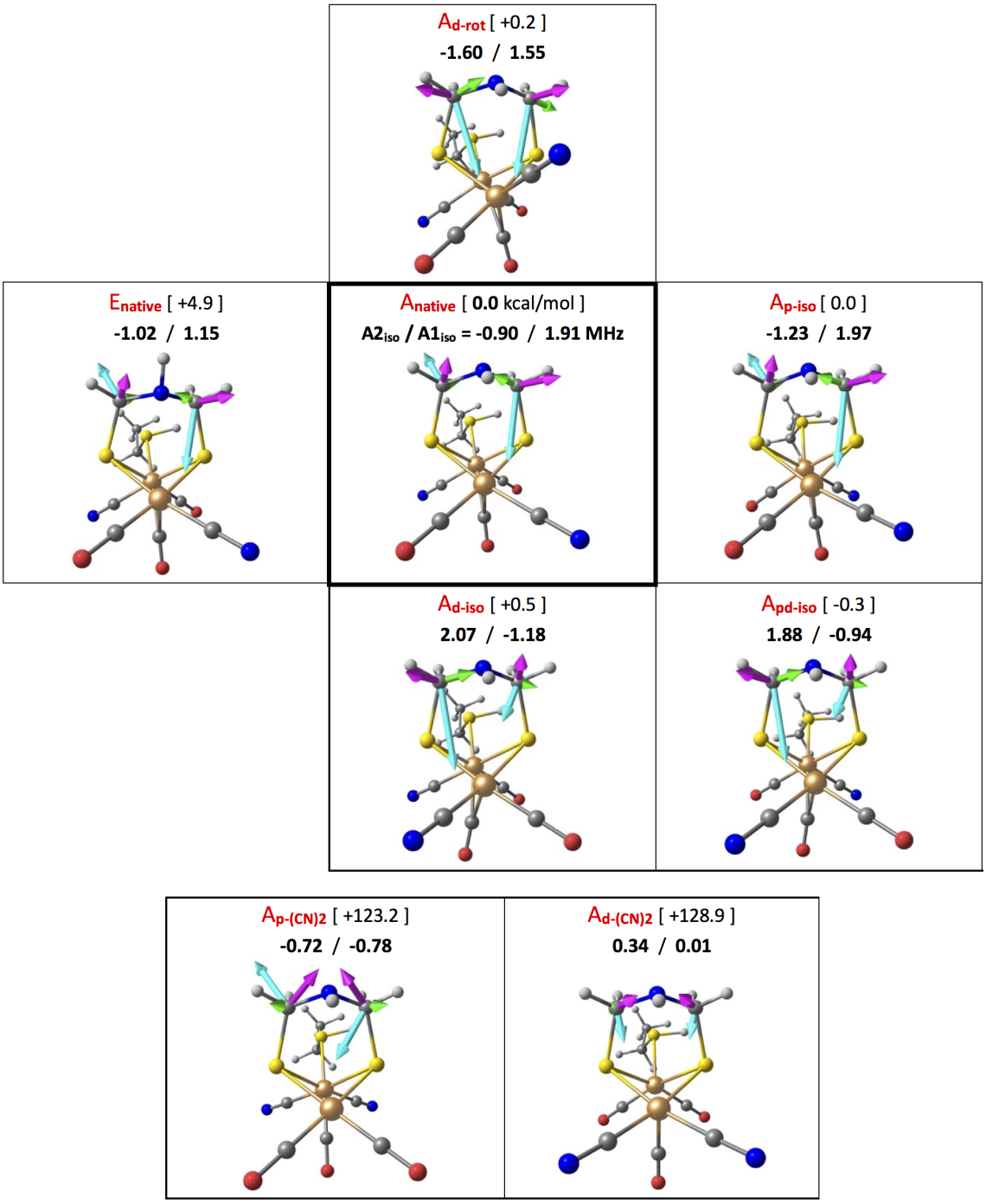


**Figure S7**. Eight isomeric $H_{ox}$ state DFT models employed in this work. The two ADT methylene $^{13}C$ nuclei anisotropic spin dipole HFI couplings in their principal axis system are provided in vector representation within the molecular frameworks; the vector lengths correspond to the conversion factor = 2Å/MHz, and the X/Y/Z axis (cf. Table S1) is colored in magenta/green/cyan, correspondingly. The calculated isotropic $^{13}C$ HFI contributions are given as $A2_{iso}$ / $A1_{iso}$ (MHz); these $^{13}C$ nuclei are correspondingly left / right in all the molecular views shown. The calculated electronic energies (kcal/mol) are provided in square brackets relatively to the representative $A_{native}$ isomer, placed centrally inside the bold frame.

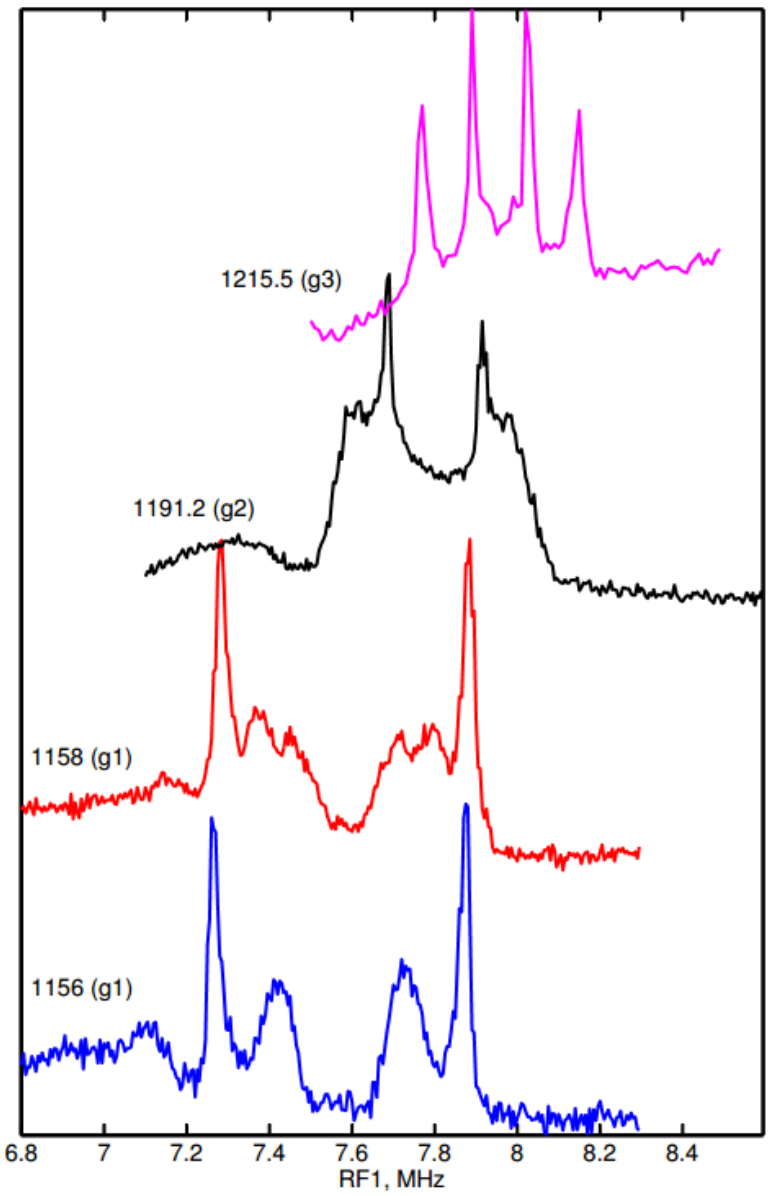


**Figure S8**. $^{2}$H-Mims-ENDOR on *Cr*HydA1 containing $^{13}$C,$^{2}$H,$^{57}$Fe-labelled ADT in the $H_{ox}$ state at different field positions given in mT along with the canonical position (g1, g2, g3), see Figure S2.

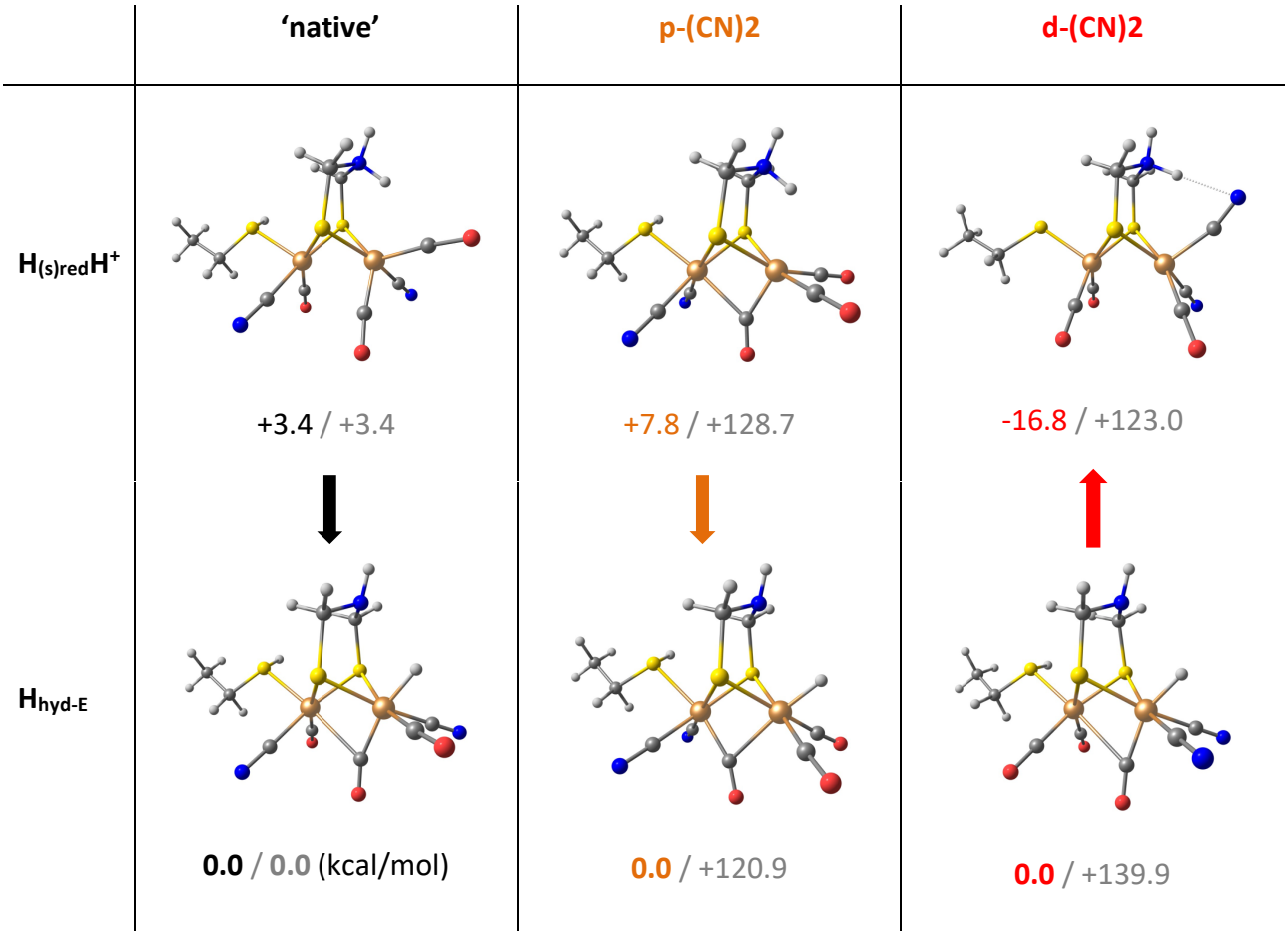


**Figure S9.** Isoelectronic and isomeric DFT models of the $H_{(s)red}H^+$ (upper row) and $H_{hyd\text{-}E}$ (lower row) intermediates of [FeFe] hydrogenase $[2Fe]_H$ subcluster with either 'native' (left) or swapped CO/CN ligand arrangements p-(CN)2 (central) and d-(CN)2 (right). The $H_{(s)red}H^+$ vs $H_{hyd\text{-}E}$ relative energies (kcal/mol) are provided in each column using uniform colors; the global relative energies of all the models vs the $H_{hyd\text{-}E}$ 'native' isomer are provided alternatively in gray; the arrows imply directions of thermodynamically favorable transformations. Notably, $H_{hyd\text{-}E}$ implies an *immediate* product of the ADT to $Fe_d$ proton transfer with its 'E' = equatorial orientation of the amine proton (vs alternative 'A' = axial proton orientation in the –NH– fragment). The CN/CO isomer labels are consistent with those used in Figure S7 and elsewhere.

## D. Supplementary Tables

**Table S1.** Experimental and DFT-predicted $^{13}C$ HFI anisotropic (X/Y/Z) and isotropic Fermi contact (iso) spin couplings (MHz) for the two methylene carbons A1 and A2 in the ADT ligand in the $H_{ox}$ state. The experimental (Exptl) and representative DFT (model $A_{native}$) values are in bold. Other values following below are from alternative isomeric DFT models shown in Figure S7. This table is an alternative representation of the data from the main text Table 1.

| | A1 (MHz) | | | | A2 (MHz) | | | |
|---|---|---|---|---|---|---|---|---|
| | *X* | *Y* | *Z* | iso | *X* | *Y* | *Z* | iso |
| **Exptl** | **-0.87** | **-0.57** | **1.43** | **1.87** | **-0.52** | **-0.26** | **0.78** | **-1.23** |
| **$A_{native}$** | **-0.71** | **-0.45** | **1.16** | **1.91** | **-0.44** | **-0.19** | **0.63** | **-0.90** |
| $E_{native}$ | -0.69 | -0.35 | 1.04 | 1.15 | -0.49 | -0.22 | 0.71 | -1.02 |
| $A_{d\text{-}iso}$ | -0.49 | -0.20 | 0.69 | -1.18 | -0.77 | -0.49 | 1.25 | 2.07 |
| $A_{p\text{-}iso}$ | -0.75 | -0.48 | 1.22 | 1.97 | -0.48 | 0.18 | 0.66 | -1.23 |
| $A_{pd\text{-}iso}$ | -0.47 | -0.18 | 0.65 | -0.94 | -0.71 | -0.46 | 1.17 | 1.88 |
| $A_{d\text{-}rot}$ | -0.71 | -0.49 | 1.20 | 1.55 | -0.71 | -0.50 | 1.21 | -1.60 |
| $A_{p\text{-}(CN)2}$ | -0.66 | -0.30 | 0.95 | -0.78 | -0.65 | -0.30 | 0.94 | -0.72 |
| $A_{d\text{-}(CN)2}$ | -0.47 | 0.07 | 0.40 | 0.01 | -0.47 | 0.04 | 0.43 | 0.34 |

**Table S2.** Mulliken atomic spin populations (in unpaired electrons) for the two H-cluster Fe sites in the presently investigated isomeric $S$ = 1/2 DFT models of the $H_{ox}$ state.

| DFT Model | Spin Population ($e^-$) | |
|---|---|---|
| | $Fe_p$ | $Fe_d$ |
| **$A_{native}$** | **0.10** | **1.00** |
| $E_{native}$ | 0.12 | 0.95 |
| $A_{d\text{-}iso}$ | 0.07 | 1.05 |
| $A_{p\text{-}iso}$ | 0.07 | 1.04 |
| $A_{pd\text{-}iso}$ | 0.10 | 1.00 |
| $A_{d\text{-}rot}$ | -0.12 | 1.22 |
| $A_{p\text{-}(CN)2}$ | 0.07 | 1.24 |
| $A_{d\text{-}(CN)2}$ | 1.08 | 0.14 |

**Table S3.** Mulliken atomic spin populations (in unpaired electrons) reflecting asymmetries at the ADT fragment and CN/CO ligands to the $Fe_d$ spin center in the $S$ = 1/2 $H_{ox}$ state, for the representative DFT model $A_{native}$. (L)eft/(R)ight in the nuclei subscript indices refers to $[2Fe]_H$ viewed as in Figure S6, right side column, and in Figure S7. Spin polarization results in e.g. left vs right / negative vs positive spin population values at the two carbon nuclei of ADT, as well as at the oxygen and nitrogen nuclei of respectively CO and CN. The table complements total spin densities shown in Figure S6.

| Nuclei | Spin Population ($e^-$) | |
|---|---|---|
| | (**L**)eft | (**R**)ight |
| $C_L$* / $C_R$* | -0.0015 | 0.0034 |
| $S_L$* / $S_R$* | -0.0132 | -0.0241 |
| $C_L$ of $C_LO_L$ / $C_R$ of $C_RN_R$ | -0.0345 | -0.0568 |
| $O_L$ of $C_LO_L$ / $N_R$ of $C_RN_R$ | -0.0067 | 0.0508 |

* Nuclei of the Fe-bound $–S_L–C_LH_2–NH–C_RH_2–S_R–$ fragment of ADT. The carbon sites $C_L$ and $C_R$ are those $^{13}C$-labeled in this study.

## References


(1) Gao, W.; Song, L. C.; Yin, B. S.; Zan, H. N.; Wang, D. F.; Song, H. B. Synthesis and Characterization of Single, Double, and Triple Butterfly 2Fe2E (E = Se, S) Cluster Complexes Related to the Active Site of FeFe - Hydrogenases. *Organometallics* **2011,** *30* , 4097-4107.

(2) Berggren, G.; Adamska, A.; Lambertz, C.; Simmons, T. R.; Esselborn, J.; Atta, M.; Gambarelli, S.; Mouesca, J. M.; Reijerse, E. J.; Lubitz, W.; Happe, T.; Artero, V.; Fontecave, M. Biomimetic Assembly and Activation of (FeFe)-Hydrogenases. *Nature* **2013,** *499*, 66-69.

(3) Reijerse, E.; Lendzian, F.; Isaacson, R.; Lubitz, W. A tunable general purpose Q-band resonator for CW and pulse EPR/ENDOR experiments with large sample access and optical excitation. *J. Magn. Reson.* **2012,** *214*, 237-243.

(4) Hyde, J. S.; Pasenkiewicz-Gierula, M.; Lesmanowicz, A.; Antholine, W. E. Pseudo Field Modulation in EPR Spectroscopy. *Appl. Magn. Reson.* **1990,** *1*, 483-496.

(5) Schweiger, A.; Jeschke, G. *Principles of Pulse Electron Paramagnetic Resonance*. Oxford University Press: Oxford, 2001.

(6) Harmer, J. R. Hyperfine Spectroscopy - ENDOR. *Emagres* **2016,** *5*, 1493-1514.

(7) Pham, C. C.; Mulder, D. W.; Pelmenschikov, V.; King, P. W.; Ratzloff, M. W.; Wang, H.; Mishra, N.; Alp, E. E.; Zhao, J.; Hu, M. Y.; Tamasaku, K.; Yoda, Y.; Cramer, S. P. Terminal Hydride Species in [FeFe]-Hydrogenases Are Vibrationally Coupled to the Active Site Environment. *Angew. Chem., Int. Ed.* **2018,** *57*, 10605-10609.

(8) Reijerse, E. J.; Pham, C. C.; Pelmenschikov, V.; Gilbert-Wilson, R.; Adamska-Venkatesh, A.; Siebel, J. F.; Gee, L. B.; Yoda, Y.; Tamasaku, K.; Lubitz, W.; Rauchfuss, T. B.; Cramer, S. P. Direct Observation of an Iron-Bound Terminal Hydride in [FeFe]-Hydrogenase by Nuclear Resonance Vibrational Spectroscopy. *J. Am. Chem. Soc.* **2017,** *139*, 4306-4309.

(9) Frisch, M. J.; Trucks, G. W.; Schlegel, H. B.; Scuseria, G. E.; Robb, M. A.; Cheeseman, J. R.; Scalmani, G.; Barone, V.; Mennucci, B.; Petersson, G. A.; Nakatsuji, H.; Caricato, M.; Li, X.; Hratchian, H. P.; Izmaylov, A. F.; Bloino, J.; Zheng, G.; Sonnenberg, J. L.; Hada, M.; Ehara, M.; Toyota, K.; Fukuda, R.; Hasegawa, J.; Ishida, M.; Nakajima, T.; Honda, Y.; Kitao, O.; Nakai, H.; Vreven, T.; Montgomery, J. A., Jr.; Peralta, J. E.; Ogliaro, F.; Bearpark, M.; Heyd, J. J.; Brothers, E.; Kudin, K. N.; Staroverov, V. N.; Kobayashi, R.; Normand, J.; Raghavachari, K.; Rendell, A.; Burant, J. C.; Iyengar, S. S.; Tomasi, J.; Cossi, M.; Rega, N.; Millam, J. M.; Klene, M.; Knox, J. E.; Cross, J. B.; Bakken, V.; Adamo, C.; Jaramillo, J.; Gomperts, R.; Stratmann, R. E.; Yazyev, O.; Austin, A. J.; Cammi, R.; Pomelli, C.; Ochterski, J. W.; Martin, R. L.; Morokuma, K.; Zakrzewski, V. G.; Voth, G. A.; Salvador, P.; Dannenberg, J. J.; Dapprich, S.; Daniels, A. D.; Farkas, Ö.; Foresman, J. B.; Ortiz, J. V.; Cioslowski, J.; Fox, D. J. *Gaussian 09, Revision D.01, Gaussian Inc., Wallingford CT, 2009*.

(10) Stephens, P. J.; Devlin, F. J.; Chabalowski, C. F.; Frisch, M. J. *Ab-initio* calculation of vibrational absorption and circular-dichroism spectra using density-functional force-fields. *J. Phys. Chem.* **1994,** *98*, 11623-11627.

(11) Becke, A. D. Density-functional thermochemistry .3. The role of exact exchange. *J. Chem. Phys.* **1993,** *98,* 5648-5652.

(12) Lee, C. T.; Yang, W. T.; Parr, R. G. Development of the Colle-Salvetti correlation-energy formula into a functional of the electron-density. *Phys. Rev. B* **1988,** *37*, 785-789.

(13) Vosko, S. H.; Wilk, L.; Nusair, M. Accurate spin-dependent electron liquid correlation energies for local spin-density calculations - a critical analysis. *Can. J. Phys.* **1980,** *58*, 1200-1211.

(14) Jaguar. *Version 9.4, Schrodinger, Inc., New York, NY, 2016.*

(15) Tomasi, J.; Mennucci, B.; Cammi, R. Quantum mechanical continuum solvation models. *Chem. Rev.* **2005,** *105*, 2999-3093.

(16) Chemcraft. - *graphical software for visualization of quantum chemistry computations.* www.chemcraftprog.com.

(17) Stoll, S.; Schweiger, A. EasySpin, a Comprehensive Software Package for Spectral Simulation and Analysis in EPR. *J. Magn. Reson.* **2006,** *178*, 42-55.